I&EC research
Industrial & Engineering Chemistry Research
pubs.acs.org/IECR

Article

Enhanced Photocatalytic Degradation of Tetracycline-Class Pollutants in Water Using a Dendritic Mesoporous Silica Nanocomposite Modified with UiO-66

Fatemeh Deymeh, Ali Ahmadpour,* Ali Allahresani, and Arash Arami-Niya*

Cite This: https://doi.org/10.1021/acs.iecr.3c02193

Read Online

ACCESS | Metrics & More | Article Recommendations

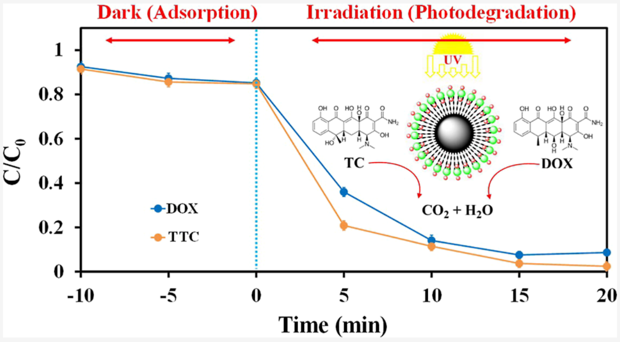

ABSTRACT: Tetracyclines (TTCs), a widely used group of antibiotics in agriculture and animal husbandry, cause water pollution and the emergence of antibiotic-resistance genes. This study reports the synthesis of a metal−organic framework nanocomposite of UiO-66 based on modified dendritic fibrous nanosilica to act as a photocatalyst for the degradation of doxycycline (DOX) and TTC as drug model pollutants in water. This nanocomposite demonstrated about three times better photodegradation performance than UiO-66 due to a decreased electron−hole recombination rate, increased conductivity, and decreased band gap, leading to the higher pollutant reduction efficiency. Structural and morphological analyses were performed on the nanocomposite, and various influencing parameters, including sample pH, catalyst dose, and irradiation time, were studied on the photocatalytic degradation of DOX and TTC to optimize the photodegradation process. At the optimum condition, the maximum photodegradation of 97.2 ± 3.1% was achieved for solutions containing 200 mg·L^{-1} each drug. The results showed that the proposed photocatalyst is stable and effective in eliminating TTC-class pollutants from water and wastewater with high efficiency and fast kinetics. The reusability of the catalyst was examined, and no significant decrease in the efficiency of the catalyst was observed after five times.

1. INTRODUCTION

The issue of water pollution has raised significant concern globally due to the presence of harmful substances like heavy metal ions,[1−4] anions,[5,6] antibiotics,[7] and dyes,.[8,9] The rapid development of industrialization has led to an increase in the quantity of these contaminants, posing substantial risks to both human health and the environment. Particularly, antibiotics, extensively used in modern medicine for an extended period, are now pervasive in the environment.[10] As these antibiotic compounds disperse and persist in the environment, they contribute to antibiotic residues, which pose a serious threat to human and ecosystem health. In recent years, the management of antibiotic contaminants in water and possible treatment methods has become a popular topic of discussion addressing this issue is crucial to safeguarding the well-being of both human populations and the delicate balance of natural ecosystems.

Doxycycline (DOX) and tetracycline (TTC) are two kinds of TTCs that are among the largest groups of antibiotics widely used in agriculture and as growth promoters in livestock farming, leading to water pollution and the emergence of antibiotic resistance genes.[11] A variety of methods, including sedimentation,[12] ion exchange,[13] reverse osmosis,[14,15] electrochemistry,[16,17] membrane separation,[18] photodegradation,[19−24] biodegradation,[25] and adsorption,[7] have been employed for the treatment of wastewater containing DOX and TTC. Among them, adsorption and photodegradation are the most proper approaches for isolating these TTC-class pollutants from water resources.[10,26] However, in the adsorption method, the adsorbents will be contaminated after the process, and various integration schemes are needed to isolate TTC-class pollutants effectively.

Heterogeneous catalytic photodegradation is a low-cost and efficient approach for the degradation of different contaminants with safe derivatives (such as CO_2, H_2O, etc.).[10] The method is based on the absorption of photons with energy levels equal to or greater than the energy of the catalytic band gap.[10] After the catalyst absorbs energy, the valence band electrons (e^-) move to the conduction band, generating

Received: June 29, 2023
Revised: August 9, 2023
Accepted: September 7, 2023

photogenic pores (h^+) in the valence band.[10] It oxidizes water molecules to produce hydroxyl radical (*OH) and superoxide radical anions ($*O_2^-$), which is an effective oxidant in the water environment. Ultimately, the generated *OH radicals can oxidatively degrade numerous organic compounds, including DOX and TTC antibiotics.[10,27]

Metal−organic frameworks (MOFs), known as coordination polymer particles and nanohybrid materials, have been developed as effective photocatalysts, and they have different applications for example water splitting, CO_2 reduction, organic conversion reactions, and decomposition of pollutants.[28−30] MOFs' high structural and compositional diversity make them attractive candidates for different applications.[28−34] The use of MOF-based hybrids in photodegradation applications has been extensively reported in recent years.[35−40] A variety of MOF shell−core nanomaterials have been recently prepared to make uniform spherical MOF nanocomposites by nucleating and growing MOFs on carboxylate or hydroxylate-modified substrates, such as silica,[41] polystyrene,[42] Fe_3O_4,[43] Al_2O_3[44] and so on. Zirconium-based MOFs such as UiO-66, commonly known for being fabricated of hexagonal zirconium clusters bound to terephthalate ligands,[45,46] were introduced as porous structures with high photocatalytic activity mainly due to their abundant active sites, extending light absorption, and effectively separating photogenerated carriers.[29,36,38]

Combining MOFs with silica could enhance the colloidal stability of MOFs, potentially leading to a reduction in their biodegradability.[47] In this regard, mesoporous fibrous nanosilica (DFNS), with unique properties and microsphere-like morphology, has been reported as effective and excellent catalyst support compared to conventional mesoporous silica materials due to its high accessible surface area and constant porosity.[48] Nevertheless, in light of DFNS neutral structure, surface modification becomes imperative to enhance its adsorptive and catalytic capabilities.[49,50] So far, various elemental, organic, and semiconductor materials, such as Ag, Al, Au, TiO_2, Fe_3O_4/SiO_2, and chitosan-oleic acid, have been employed to enhance the surface properties of DFNS.[49]

This study aimed to investigate the feasibility of nucleation and growth of UiO-66 on the surface of amine-modified DFNS to develop an advanced heterostructured photocatalyst for the photodegradation of DOX and TTC under UV light. Through the synthesis of UiO-66@NH_2-DFNS nanocomposites, the ordered microporosity of UiO-66 MOF and the mesoporosity of DFNS can be combined. The success of the proposed UiO-66@NH_2-DFNS synthesis was investigated, and its potential was evaluated for the photodegradation of DOX and TTC contaminants from aqueous media. The effects of various variables, including sample pH, catalyst dose, and irradiation time, on the photocatalytic degradation of DOX and TTC were analyzed using the response surface methodology. Additionally, the photodegradation mechanism of DOX and TTC was investigated to enhance the photocatalytic performance of UiO-66@NH_2-DFNS.

2. MATERIALS AND METHODS

2.1. Chemicals. Cetyltrimethylammonium bromide ($C_{19}H_{42}BrN$), urea (CH_4N_2O), 3-aminopropyl triethoxysilane (APTES, $C_9H_{23}NO_3Si$), tetraethyl orthosilicate (TEOS, $SiC_8H_{20}O_4$), zirconium tetrachloride ($ZnCl_4$), 1,4-benzenedicarboxylic acid (terephthalic acid, $C_8H_6O_4$), *N*,*N*-dimethylformamide (DMF, C_3H_7NO), chloroform ($CHCl_3$), cyclohexane (C_6H_{12}), 1-pentanol ($C_5H_{11}OH$), and ethanol (C_2H_6O) of analytical and synthesis grades were procured from Merck Co. (Germany). DOX and TTC, both with a purity of at least 98%, were acquired from Sigma-Aldrich Co. (USA). The solutions were freshly prepared each day using distilled water (DDW). The pH of the prepared solutions was adjusted using hydrochloric acid and sodium hydroxide solutions (1.0 M) sourced from Merck (Germany).

2.2. Synthesis of UiO-66@NH_2-DFNS. The DFNS sample was prepared using the hydrothermal approach:[48,51] The method of compound synthesis is described in a study by Deymeh et al.[24] UiO-66 was synthesized through a solvothermal method:[29] Initially, a 100 mL Schott bottle was filled with 10 mL of DMF, followed by the dissolution of 0.7 g of terephthalic acid and 0.5 g of $ZrCl_4$ at 80 °C for 30 min. The solution was clarified in an ultrasonic bath and then transferred to a stainless-steel Teflon-lined autoclave, which was placed in an oven at 120 °C for 24 h. After cooling, the sample underwent three centrifugation cycles with DMF to eliminate any residual reactants, followed by additional cycles with absolute methanol to remove DMF. The resulting powder was soaked in fresh DMF for 1 h and in methanol for 24 h and subsequently vacuum-dried overnight at 70 °C.

To create the final composite, 0.5 g of $ZrCl_4$ and 1.5 g of NH_2-DFNS were combined with 10 mL of DMF in a vial, heated to 80 °C (refer to Figure 1). In a separate vial, 0.7 g of terephthalic acid was dissolved in 10 mL of DMF at the same temperature. The prepared solutions were mixed and subjected to ultrasonic vibration for 30 min. The resulting mixture was then placed in a stainless-steel Teflon-lined autoclave and maintained at 120 °C for 24 h. Following this, the autoclave was cooled to room temperature, and the produced UiO-66@NH_2-DFNS nanoparticles were filtered, washed multiple times with DMF and $CHCl_3$, and finally dried at 80 °C using a vacuum oven.

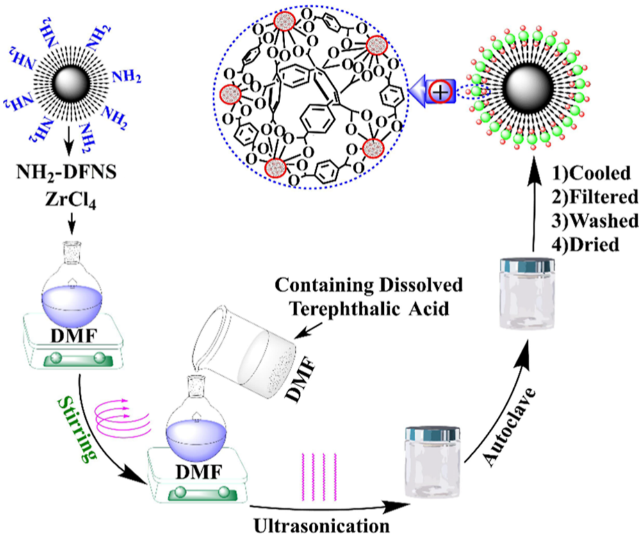

Figure 1. Synthesis of UiO-66@NH_2-DFNS.

2.3. Characterization of the Materials. The surface characteristics and morphology of synthesized UiO-66@NH_2-DFNS were examined using various analytical techniques. These included a scanning electron microscope equipped with energy-dispersive X-ray analysis (SEM−EDX, TECSAN VEGA3 model from Czech Republic), a high-resolution transmission electron microscope (TEM, ZEISS LIBRA 200 FE from Germany), N_2 adsorption at 77 K (BELSORP MINI from Osaka, Japan), X-ray diffraction (XRD, Bruker AXS-D8 Advance from the USA) with Cu Kα radiation, X-ray photoelectron spectroscopy (XPS, Thermo Scientific Nexsa G2 from USA), and thermogravimetric analysis (TGA, Q600 from TA Instrument, the USA).

The collected N_2 adsorption/desorption data were analyzed using the Brunauer−Emmett−Teller (BET) model, and the resulting BET surface area was reported for P/P_0 = 0.050−0.982 (BELSORP MINI, Osaka, Japan). Additionally, the functional groups' type and quality were identified using Fourier-transform infrared (FTIR) spectroscopy (PerkinElmer Spectrum 65 from the USA) in the wavenumber range of 4000 to 400 cm^{-1}. To determine the concentrations of DOX and TTC, a UV−vis spectrophotometer (AnalyticJena Specord 210 from Germany) and an HPLC system (Agilent 1200 from USA) were employed.

2.4. Photodegradation Experiments. For initial investigations into adsorption-photodegradation, a uniform dispersion of 20 mg of UiO-66@NH_2-DFNS nanocomposites was created in vials containing 10 mL of 100 mg·L^{-1} DOX and TTC. The mixture was stirred in darkness for 0 to 10 min to establish an adsorption−desorption equilibrium. Subsequently, the suspension within the reactor was subjected to an UV lamp radiation for varying durations (0 to 20 min) to study the photodegradation characteristics of the prepared samples. To eliminate UiO-66@NH_2-DFNS nanoparticles, centrifugation was conducted at 9000 rpm for 10 min. The efficiency of degradation was determined by measuring the liquid's absorbance using an UV−vis spectrophotometer at specific wavelengths: 275 nm for DOX and 357 nm for TTC. The remaining quantities of DOX and TTC in the samples were quantified through chromatographic analysis using an Agilent 1200 HPLC system.

2.5. Modeling and Optimization Process. The chemometric approach involved utilizing a central composite design (CCD) within the framework of the response surface method, as outlined in ref 52. Experimental data analysis was carried out using Design-Expert software (Trial Version 12, Stat-Ease, Inc., Minneapolis, USA). The effects of three independent factors, namely, sample pH, UiO-66@NH_2-DFNS dose (mg·mL^{-1}), and irradiation time on the photodegradation process, were meticulously examined using the CCD. The degradation of DOX and TTC was identified as the desired outcomes for the proposed models. The three chosen variables (designated as A−C) were converted into coded values at levels of −1.68, −1, 0, +1, and +1.68, as documented in Table 1.

3. RESULTS AND DISCUSSION

After synthesizing DFNS, UiO-66, and UiO-66@NH_2-DFNS, the prepared materials' properties and photocatalytic performance were assessed and compared with the literature, as described in the following sections. Before the use of synthesized substrates, synthesized catalysts were identified using FTIR, XRD, diffuse reflectance spectroscopy (DRS), BET, TGA, SEM−EDX, TEM, and XPS. Also, its zeta-potential charge was determined to illustrate how UiO-66@NH_2-DFNS nanocomposite interacts with negatively charged species.

Table 1. Experimental Parameters and Their Levels for the CCD Matrix

parameters	levels				
	$-\alpha$	−1	0	+1	$+\alpha$
A: sample pH	2.0	3.0	4.5	6.0	7.0
B: UiO-66@NH_2-DFNS dose (mg mL^{-1})	0.32	1.0	2.0	3.0	3.68
C: radiation time (min)	3.2	10	15	20	36.8

3.1. Characterization. FTIR analysis serves as an effective method for examining surface functional groups in materials. In this study, transparent tablets were prepared using KBr to investigate the FTIR spectra and identify the functional groups present in the synthesized materials including DFNS, NH_2-DFNS, UiO-66, and UiO-66@NH_2-DFNS. The FTIR spectra for these synthesized substances are presented in Figure 2. For DFNS and NH_2-DFNS, the spectral bands within the range of 3440−3220 cm^{-1} corresponded to the O−H stretching band, while the O−H bending vibration manifested at 1632 and 1630 cm^{-1}, respectively. Bands around 1090−1200 cm^{-1} indicated the asymmetric stretching of Si−O−Si, with a peak at 816 cm^{-1} signifying symmetric vibrations of Si−O−Si in both DFNS and NH_2-DFNS.

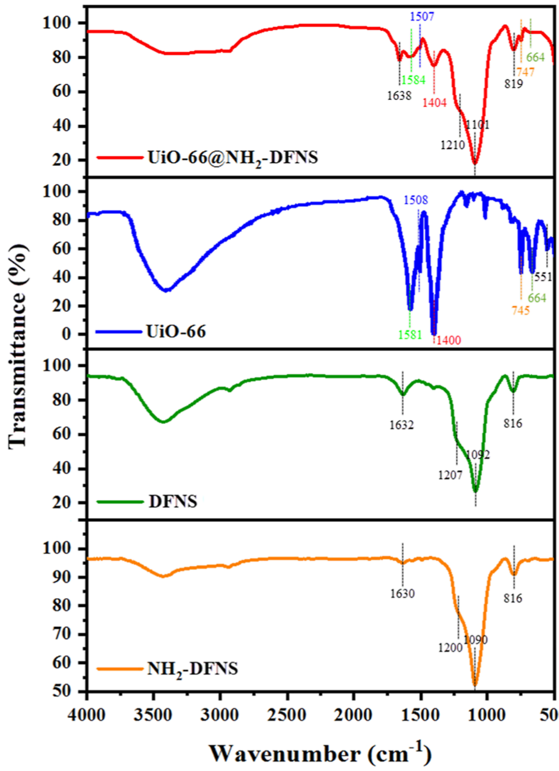

Figure 2. FTIR spectra of the synthesized DFNS, NH_2-DFNS, UiO-66, and UiO-66@NH_2-DFNS.

Within the FTIR spectra of UiO-66@NH_2-DFNS, these bands were observed at 1638, 1210, 1101, and 819 cm^{-1}, indicating the presence of DFNS within the nanocomposite. Moreover, absorption bands around 1580 and 1400 cm^{-1} were attributed to the asymmetric and symmetric stretching vibration of carboxylate groups in the terephthalic ligands within the UiO-66 structure.[29] Notably, a weak band related to the C=C vibration of the benzene ring appeared at approximately 1507 cm^{-1} for both UiO-66 and UiO-66@NH_2-DFNS.[29] Additionally, a band at around 745 cm^{-1} was linked to the C−H vibrations of the ligands within the UiO-66 structure. The stretching vibration band at 664 cm^{-1}, present in both UiO-66 and UiO-66@NH_2-DFNS, was attributed to Zr−O within the MOF structure.[29] These findings collectively confirm the stable integration of UiO-66 onto the NH_2-DFNS surface.

Figure 3 displays the arrangement of XRD at the 2θ scope of 5−80° for DFNS and UiO-66@NH_2-DFNS. The wide peak observed between 2θ = 15−30° for both DFNS and UiO-66@NH_2-DFNS samples indicates the presence of amorphous silica.[53] Furthermore, the emergence of new peaks at 2θ = 7.7, 8.8, 12.3, 22.6, 26.1, 31.2, 44.0, and 51.1° in the XRD pattern of UiO-66@NH_2-DFNS corresponds to those found in other literature reports on UiO-66-based heterojunction photocatalysts.[29,38] This alignment underscores the successful immobilization of UiO-66 on the surface of NH_2-DFNS.

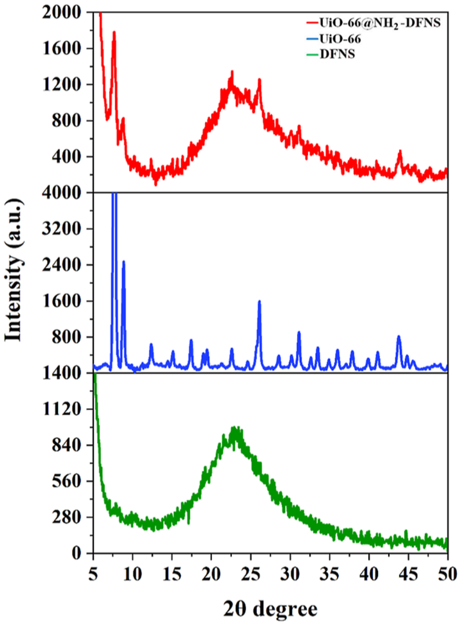

Figure 3. XRD pattern for the synthesized DFNS, UiO-66, and UiO-66@NH_2-DFNS.

The UV−vis DRS of the UiO-66@NH_2-DFNS nanocatalyst was performed to specify the band gap energy (E_g). Light containing energy $h\upsilon$ can pass through, reflect, or be absorbed by a material depending on the magnitude of the energy. If the energy of the incident photons is lower than the energy of the band gap, the light will pass through the material, but if the energy of the band gap is higher, the light will be absorbed. E_g can be calculated using the absorption coefficient, α, in the Tauc eq (eq 1).[54]

$$\alpha h\upsilon = A(h\upsilon - E_g)^m \tag{1}$$

where α is the absorption coefficient, A is a constant, $h\upsilon$ is photon energy, and E_g is band gap energy. m value of 0.5 is considered direct, and a m value of 2.0 (eq 2) is an indirect transition type.

$$h\upsilon = (\alpha h\upsilon)^2 \tag{2}$$

The band gap energy can be calculated by extrapolating the linear section of the $(\alpha h\upsilon)^m$ with a horizontal axis $h\upsilon$ plot (Figure 4), as E_g = 3.36 eV.[55] Even though DFNS and UiO-66 alone have relatively wide band gap energies, i.e., 4.04 and 3.60 eV, respectively,[24,29,55,56] the proposed UiO-66@NH_2-DFNS appears to have a narrower band gap, thus can utilize effective photodegradation response under lower energy radiation.[24,29,55,56]

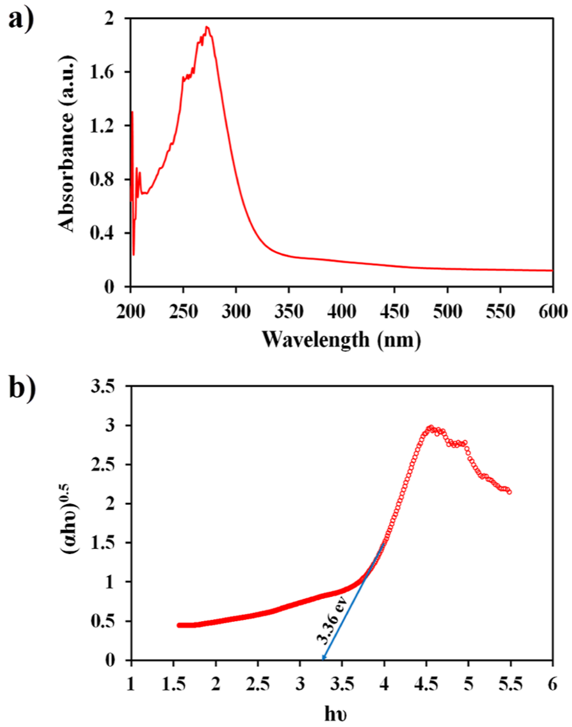

Figure 4. (a) UV−vis and (b) DRS for UiO-66@NH_2-DFNS.

Specific surface area and pore dimensions of UiO-66@NH_2-DFNS were specified by employing a nitrogen adsorption/desorption isotherm (Figure 5a). The UiO-66@NH_2-DFNS exhibit type IV isotherms, indicating a typical mesoporous structure, with unlimited monolayer-multilayer adsorption for

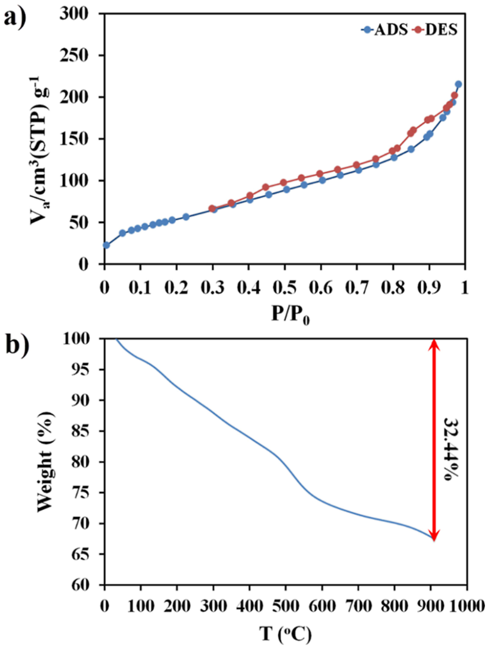

Figure 5. (a) Nitrogen adsorption−desorption isotherm at 77 K and (b) TGA plot for UiO-66@NH_2-DFNS.

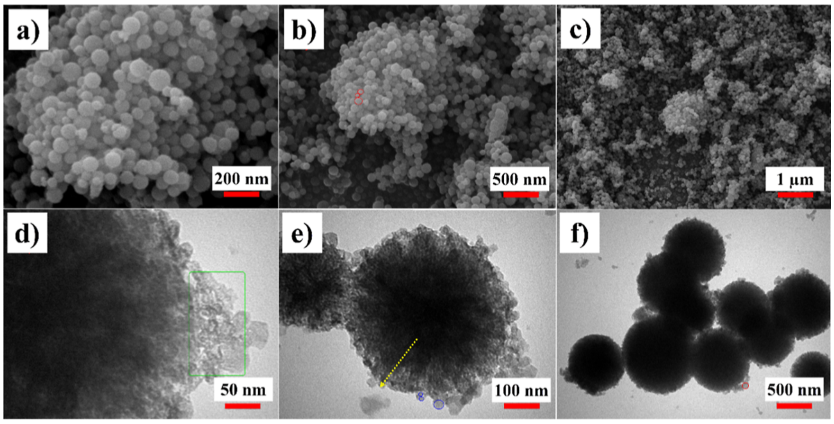

Figure 6. SEM (a−c) and TEM (d−f) images for the synthesized UiO-66@NH_2-DFNS.

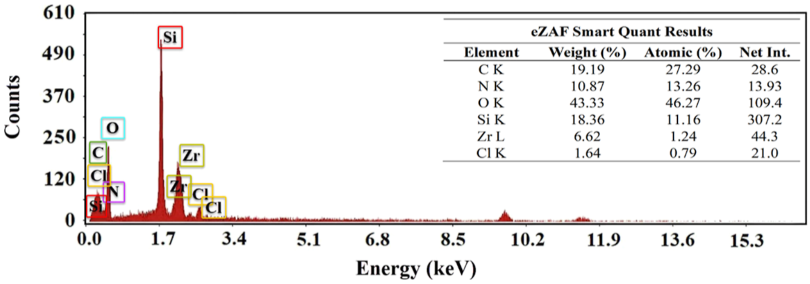

eZAF Smart Quant Results

Element	Weight (%)	Atomic (%)	Net Int.
C K	19.19	27.29	28.6
N K	10.87	13.26	13.93
O K	43.33	46.27	109.4
Si K	18.36	11.16	307.2
Zr L	6.62	1.24	44.3
Cl K	1.64	0.79	21.0

Figure 7. SEM−EDX analysis of the proposed UiO-66@NH_2-DFNS nanocomposite.

nitrogen adsorption at 77 K (Figure 5a).[47,57−59] In the first step, at low relative pressures, the adsorption volume increases due to the interaction of the nitrogen molecules with the more energetic section.[58] The showed rise in relative pressure, at $P/P_0 = 0.45$, relates to multilayer formation when the monolayer formation of the adsorbed molecules is complete.[57,60−63] Another rise in relative pressure, at $P/P_0 = 0.85$, indicates the bulk condensation of adsorbate nitrogen gas.[57,60−63] This indicates capillary nitrogen condensation within the uniform mesopores. A significant shift in the adsorption branches toward lower relative pressures was also observed. Hysteresis typically manifests when evaporation takes place within mesopores, leading to desorption occurring in a lower-pressure region compared to capillary condensation. As it is clear from Figure 5a, the H3 hysteresis loop of the UiO-66@NH_2-DFNS has a similar mesoporous structure as DFNS. At $P/P_0 = 0.982$, the total pore volume was 0.3325 $cm^3 \cdot g^{-1}$. Based on *t*-plot calculations, the volume of micropores was 0.1207 $cm^3 \cdot g^{-1}$, so a total of 36.3% of porosity can be attributed to micropores.[47] Finally, the BET surface area of about 199.3 $m^2 \cdot g^{-1}$ demonstrates that the UiO-66@NH_2-DFNS could be a suitable substrate for the catalyst.[47,58]

The thermal stability of UiO-66@NH_2-DFNS was determined by TGA analysis under a nitrogen atmosphere with a heating rate of 10 °C min^{-1} in the temperature range of 30−900 °C (Figure 5b). The TGA of UiO-66@NH_2-DFNS shows three stages of weight loss of about 32%. Before 100 °C, a partial mass change of 7% was observed in the TGA curve of the UiO-66@NH_2-DFNS nanocatalyst, which indicates the presence of physically adsorbed water molecules. The second mass loss of less than 5% at 150−200 °C is attributed to the decomposition of DMF.[64] The third rapid mass loss at about 470−530 °C is attributed to the decomposition of Zr-ligands in the UiO-66 structure to ZrO_2.[64] Therefore, the prepared UiO-66@NH_2-DFNS nanocatalyst is thermally stable below 470 °C.

The exterior surface morphology and elemental examination of UiO-66@NH_2-DFNS were determined by TEM, SEM, and EDX analyses (Figures 6 and 7). The morphology of UiO-66@NH_2-DFNS is typical of DFNS-corresponding spherical nanoparticles with a homogeneous particle size distribution (some are illustrated as red circles in Figure 6b).[65] Figure 6d,e obviously indicates the mounted UiO-66 crystalline shells on spherical DFNS nanoparticles.[66] Hollow-nature of the spherical DFNS nanoparticles is revealed by the contrast between the dark center and the pale edge in the nanospheres (some shown as blue circles in Figure 6e).[65] Figure 6d, demonstrates that the UiO-66 shells are porous structures with estimated pore sizes of below 10 nm. UiO-66 nanocrystal aggregation is also portrayed as a green rectangle.[66] The UiO-66 nanocrystals grew inside and outside the pores of DFNS, forming a layer on the DFNS surface in which the growth path was demonstrated as a yellow dashed arrow.[67] On the surface of DFNS, the UiO-66 nanocrystals did not grow further due to the high concentration of Zr-ligands used, but it sounds like the UiO-66 nanocrystals gradually fill the gaps between the crystals.[67] The thickness of the UiO-66 layer increased as the gaps in the UiO-66@NH_2-DFNS spheres were continuously filled with UiO-66 nanocrystals, resulting in core−shell spheres in the UiO-66@NH_2-DFNS which is obvious in TEM images (see Figure 6d,e). Also, the presence of Zr on UiO-66@NH_2-DFNS indicates the successful modification of DFNS with UiO-66 (Figure 7). These results confirm the chemical bonding of UiO-66 to the NH_2@DFNS outer layer and the production of a nanocatalyst with a consistent and uniform size (average size = 103 nm).

The elemental composition of the prepared Ui-O66@NH_2-DFNS nanocatalyst was analyzed by XPS, and the results are

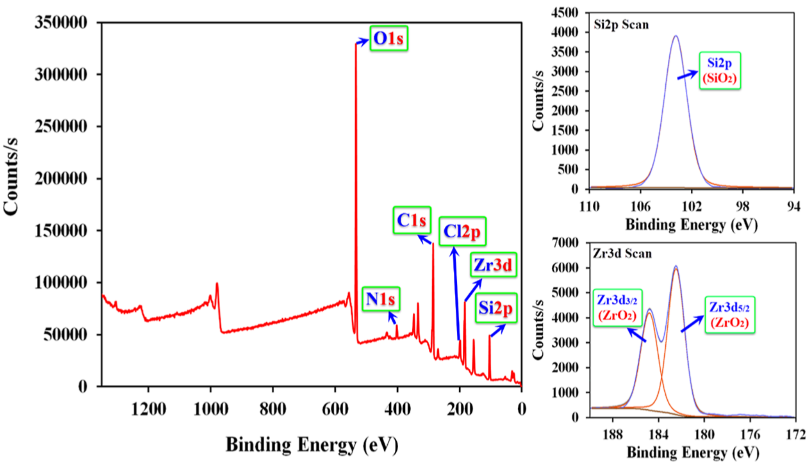

Figure 8. XPS analysis (XPS survey, Zr 3d scan, and Si 2p scan) for the synthesized UiO-66@NH$_2$-DFNS nanocatalyst.

presented in Figure 8. The scanning spectrum confirmed the presence of Si, Zr, Cl, C, N, and O in the Si$_{2p}$, Zr$_{3d}$, Cl$_{2p}$, C$_{1s}$, N$_{1s}$, and O$_{1s}$ binding energy zones of the fabricated Ui-O66@NH$_2$-DFNS. Si$_{2p}$ and Zr$_{3d}$ revealed peaks at 103.32 and 182.57 eV for O−Si−C and O−Zr−C bonds, respectively.[68] The C−C, C═O, and C═N−C bonds were revealed at 284.67 eV, and the Cl$_{2p}$ peak at 198.18 eV corresponded to metal−Cl.[69,70] The peak corresponding to N$_{1s}$ appeared at 401.52 for N−H in the UiO-66@NH$_2$-DFNS structure.[68] The O$_{1s}$ peak is shown to be 532.46 for Zr−O and Si−O−C.[68,71] Also, the high-resolution XPS data in the zone of Zr$_{3d}$ showed two peaks, paralleling the 3d$_{3/2}$ and 3d$_{5/2}$ ZrO$_x$.

Finally, the zeta-potential charge and mobility of UiO-66@NH$_2$-DFNS were also analyzed and found to be 7.68 mV and 0.6017 μm cm/(V s), respectively. It indicates a tendency of UiO-66@NH$_2$-DFNS nanocomposites to interact with negatively charged species.[72]

3.2. Photocatalytic Activity.

The preliminary investigations on the adsorption and photodegradation characteristics of the nanocomposites were conducted based on the procedure described in Section 2.4. Based on the results demonstrated in Figure 9, less than 16% of DOX and TTC were initially removed in the first 10 min under dark conditions, primarily attributable to surface adsorption, with no involvement of photodegradation. Using 2.0 mg mL^{-1} UiO-66@NH$_2$-DFNS resulted in a photodegradation efficiency above 90% after 20 min irradiation. This value was about 15% for DFNS, 25% for NH$_2$-DFNS, attributed to H-bonding adsorptive interactions, and 54−58% for UiO-66. The higher photodegradation efficiency of UiO-66@NH$_2$-DFNS and UiO-66 under UV light in comparison with DFNS and NH$_2$-DFNS confirms the presence of UiO-66 alone, or its immobilized sample on the NH$_2$-DFNS surface had a significant impact on its photodegradation properties.

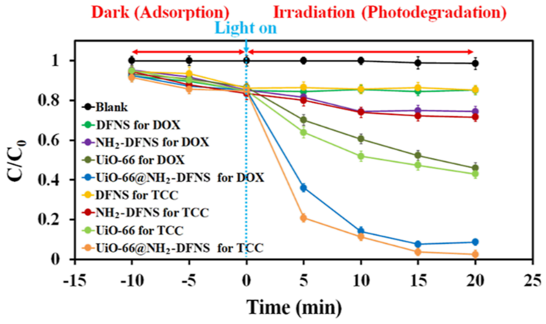

Figure 9. Effect of irradiation time on the DOX and TTC photodegradations using DFNS, NH$_2$-DFNS, UiO-66, and UiO-66@NH$_2$-DFNS. Process condition: photocatalyst dose = 2.0 mg·mL^{-1}, DOX and TTC concentration = 100 mg·L^{-1}.

The effect of reactive oxygen was analyzed by using H$_2$O$_2$ as reactive oxygen species, and the experiments were performed with and without H$_2$O$_2$. As illustrated in Figure 10, there is no significant difference in the DOX and TTC photodegradation of the experiments. As a result, there is no need to add H$_2$O$_2$ to the solution when using the proposed UiO-66@NH$_2$-DFNS.

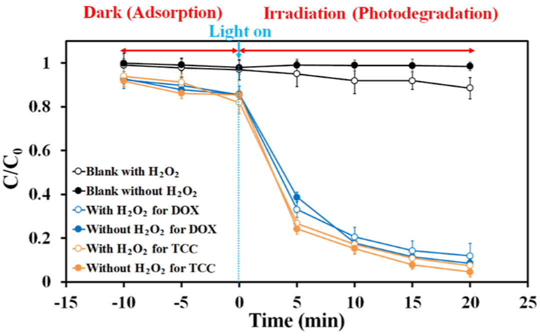

Figure 10. Effect of H$_2$O$_2$ on the DOX and TTC photodegradations using UiO-66@NH$_2$-DFNS. Process condition: photocatalyst dose = 2.0 mg·mL^{-1}, DOX and TTC concentration = 100 mg·L^{-1}.

3.3. Modeling and Optimization.

The effect of different variables of the sample pH, nanocatalyst dose, and irradiation time on the photodegradation of DOX and TTC using UiO-66@NH$_2$-DFNS was investigated by employing a CCD-based template. The developed model was assessed by employing an analysis of variance (ANOVA). Considering the restricted number of variables to be optimized, only CCD was applied, and the screening was skipped. The CCD tests were performed based on the software design matrix for solutions containing 200 mg·L^{-1} DOX and TTC. The following coded quadratic polynomial model for the average photodegradation of DOX and TTC was derived by ANOVA and CCD methods.

Table 2. ANOVA for Photodegradation Efficiencies Using UiO-66@NH_2-DFNS

source	SS[a]	df[b]	MS[c]	F-value	p-value	
model	13043.93	9	1449.33	273.11	<0.0001	S[e]
A: sample pH	2089.73	1	2089.73	393.78	<0.0001	”
B: UiO-66@NH_2-DFNS	4759.58	1	4759.58	896.88	<0.0001	”
C: irradiation time	2127	1	2127	400.8	<0.0001	”
AB	87.12	1	87.12	16.42	0.0019	”
AC	359.12	1	359.12	67.67	<0.0001	”
BC	0.02	1	0.02	0.0038	0.9521	NS[f]
A^2	766.86	1	766.86	144.5	<0.0001	S[e]
B^2	1780.82	1	1780.82	335.57	<0.0001	”
C^2	1129.49	1	1129.49	212.84	<0.0001	”
residual	58.38	11	5.31			
LOF[d]	41.34	5	8.27	2.91	0.1128	NS[f]
pure error	17.03	6	2.84			
cor total	13135.71	22				

[a] Sum of squares. [b] Degree of freedom. [c] Mean square. [d] Lack of fit. [e] Significant. [f] Not significant.

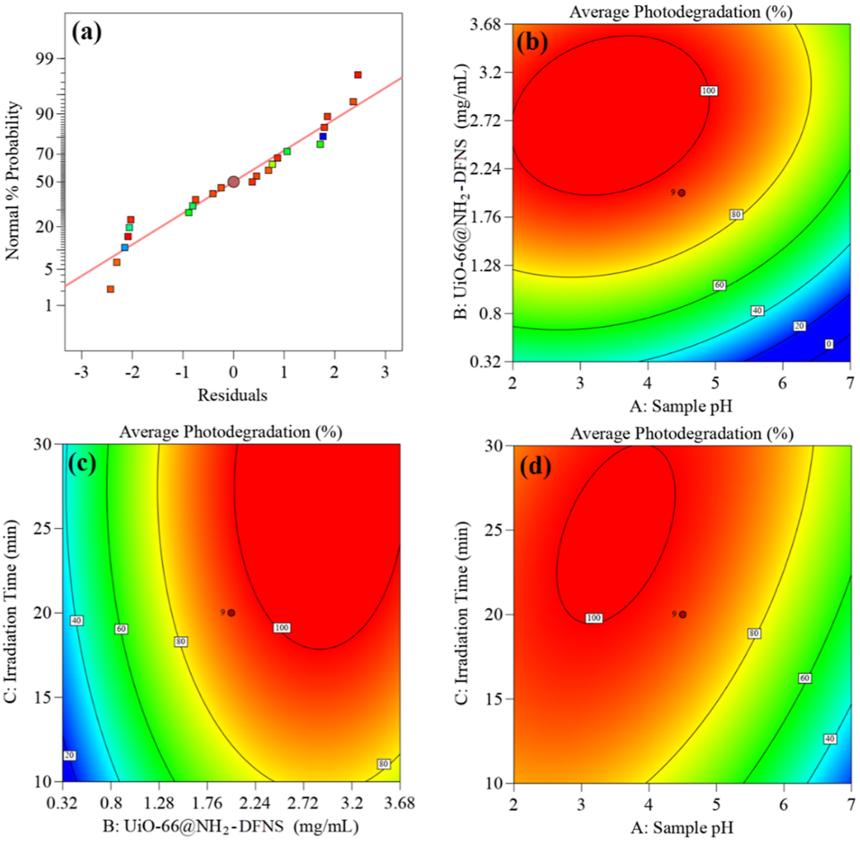

Figure 11. Normal probability (a) and response surface (b−d) plots for average photodegradation.

$$\text{Degradation }(\%) = 94.9 - 12.4\text{A} + 18.7\text{B} + 12.5\text{C} + 3.3\text{AB} + 6.7\text{AC} - 0.05\text{BC} - 6.9\text{A}^2 - 10.6\text{B}^2 - 8.4\text{C}^2 - 5.7\text{D}^2 \qquad (3)$$

Positive and negative effects of each variable on the average photodegradation response are well-defined at this equation with positive and negative signs. For both TTC-class pollutants under investigation, the effect of the sample pH on photodegradation was negative. However, the nanocomposite dose and irradiation time positively influenced photodegradation. The ANOVA results of average photodegradation (Table 2) were on the basis of F-values and the mean squares employed to predict the influence of the model and each variable in comparison with residuals. The F-value of 273.11 was statistically significant. A lake of fit F-value of 2.91 revealed the reliability of the model, showing that the omitted terms were nonsignificant.[7]

The R^2 value of 0.9955 mirrored the concurrence between the experimental and estimated outcomes. In addition, the predicted R^2 of 0.9717 is in appropriate accordance with the adjusted R^2 of 0.9926 as it differed by around 2%. The normal probability of the residuals (Figure 11) revealed that residuals were randomly distributed around zero, indicating the model's reliability.[7] This acceptable normal distribution confirms the validity of the assumptions and independency behavior in residuals.

The response surface graphs of the proposed model were employed to examine the interactions between the variables and portray their impact on photodegradation. As shown in Figure 11, the pH-dose and pH-irradiation times affirmed strong interactions, as evidenced in the ANOVA table (Table 2). In addition, a deeper attention at these graphs illustrated that decreasing the sample pH and increasing the UiO-66@NH_2-DFNS dose and irradiation time increased the photodegradation efficiency. Meanwhile, the sample pH values lower than 5 showed acceptable photodegradation with moderate values of dose and time.

The photodegradation process was influenced positively by the dose of the nanocomposite and irradiation duration. Notably, the UiO-66@NH_2-DFNS dose had a more significant impact than the irradiation time. On the other hand, the pH of the sample had a negative effect on the photodegradation efficiency, except for pH values below 5.0, which maintained consistent efficiency.

A change in the pH of solution can affect the surface charge of UiO-66@NH_2-DFNS, its photocatalytic capacity, and DOX/TTC ionization state, so pH is a crucial factor in the degradation process.[73,74] At pH values lower than 5.0, the number of hydrogen bonds between DOX/TTC and UiO-66@NH_2-DFNS increased the catalytic decomposition rate, promoting the relocation of antibiotics from the solution to the UiO-66@NH_2-DFNS outer layer. As shown in Figure 11b,d, the UiO-66@NH_2-DFNS photocatalytic system demonstrated excellent efficiency even under acidic pH conditions. This can be attributed to its interactions with negatively charged species, as revealed in the zeta-potential analysis discussed in Section 3.1.

The pH also influenced the ionization state of DOX (pK_a = 3.09)/TTC (pK_a = 3.26), affecting the electrostatic forces between the molecules and the photocatalyst.[73,74] At pH below 3.0, DOX/TTC was mostly protonated, leading to strong electrostatic repulsion by the UiO-66@NH_2-DFNS photocatalyst. At pH 3.0−5.0, the neutral forms (zwitterions) of DOX/TTC increased, resulting in better photocatalytic performance due to reduced electrostatic repulsion and enhanced hydrogen bonding forces. However, at pH over 5.0, the role of hydrogen bonding forces decreased, and the efficiency decreased significantly.

To confirm these findings, experiments were conducted at pH = 8.0, resulting in a significant decrease in the photodegradation efficiency for solutions containing 200 mg·L^{-1} DOX and TTC (47.1 ± 8.5%). It is likely that at pHs above 7.0, anionic DOX/TTC molecules were attracted electrostatically by UiO-66@NH_2-DFNS, but the hydrogen bonding forces, which were at their lowest level, played a more predominant role, leading to the observed decrease in the efficiency.

A nonlinear optimization approach following the Nelder−Mead algorithm defined the optimum condition to achieve maximum photodegradation (95.7 ± 2.2%) for solutions containing 200 mg·L^{-1} DOX and TTC, pH = 4.2, nanocomposite quantity = 2.9 mg mL^{-1}, and irradiation time = 30 min. The experimental tests at the optimized conditions achieved an average photodegradation of 97.2 ± 3.1, showing an excellent agreement between the experimental and CCD model's predicted data.

3.4. Kinetic Investigations. The rate of kinetic photodegradation of DOX and TTC under UV light was investigated within the predetermined optimal conditions. By utilizing the identified best-case scenario, the data obtained from the photodegradation process of DOX and TTC were fitted to the linearized integrated forms of the zero-order (eq 4), pseudo-first-order (eq 5), and pseudo-second-order (eq 6) kinetic models.[75]

$$C_0 - C_t = k_{\mathrm{app}}t \tag{4}$$

$$\ln\left(\frac{C_0}{C_t}\right) = k_{\mathrm{app}}t \tag{5}$$

$$\frac{1}{C_t} - \frac{1}{C_0} = k_{\mathrm{app}}t \tag{6}$$

where k_{app} is the apparent rate constant generated by k_{obs} and K_{an}, k_{obs} is the rate constant, K_{an} is the adsorption−desorption equilibrium constant, and C_0 and C_t (mg·L^{-1}) are antibiotic concentration at initial and time t.

Using eq 5, the linearized graphs for the photodegradation kinetics of DOX and TTC employing UiO-66@NH_2-DFNS nanocatalysts are portrayed in Figure 12. According to this figure, the pseudo-first-order kinetic model with R^2 values of 0.9953 and 0.9989 for DOX and TTC fully defined the photodegradation procedure. Moreover, as shown in Table 3, the k_{app} values presented from the slope of the graphs for DOX and TTC photodegradation are 0.0929 and 0.1209 min^{-1}, respectively. The k_{app} values revealed a higher TTC photodegradation rate than that of the DOX degradation (see Table 3).

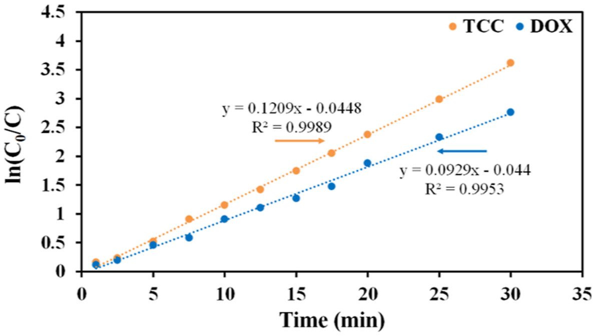

Figure 12. Kinetic fits of pseudo-first-order for DOX and TTC photodegradation by UiO-66@NH_2-DFNS. Process condition: sample pH = 4.2, photocatalyst dose = 2.9 mg mL^{-1}, DOX and TTC concentration = 200 mg·L^{-1}.

3.5. Probable Implemented Mechanism. As shown in Section 3.2 and Figure 9, the photodegradation of 100 mg·L^{-1} solutions of DOX and TTC in the presence of UiO-66@NH_2-DFNS under UV irradiation can reach 95% in only 20 min. Superoxide ($O_2{}^{*-}$) and hydroxyl (OH^*) radicals, along with electrons (e^-) and/or holes (h^+), can contribute to photo-assisted oxidation of DOX and TTC. The e^- and h^+ are formed in a semiconductor when the energy is greater than the band gap, allowing a heterogeneous photocatalysis reaction. The OH^* can be produced by reacting surface adsorbed water [$(H_2O)_{\mathrm{ads}}$] with valence band holes (h_{VB}). Also, the H_2O_2 molecules can increase the concentration of the produced OH^* species. In addition, dissolved O_2 can interact with electrons in conduction bonds to produce $O_2{}^{*-}$. To determine

Table 3. Kinetic Parameters for DOX and TTC Photodegradation by UiO-66@NH$_2$-DFNS[a]

antibiotic	zero-order		pseudo-first order		pseudo-second order	
	k_0 (mg·L^{-1}·min^{-1})	R^2	k_1 (min^{-1})	R^2	k_2 (L·mg^{-1}·min^{-1})	R^2
DOX	5.8335	0.9018	0.09295	0.9953	0.0021	0.8371
TTC	5.7945	0.8378	0.12091015	0.9989	0.0048	0.7672

[a] Process condition: sample pH = 4.2, photocatalyst dose = 2.9 mg·mL^{-1}, DOX and TTC concentration = 200 mg·L^{-1}.

the role of these reactive species in photodegradation experiments, various scavengers such as 1,4-benzoquinone, 2-propanol, silver nitrate, and triethylamine were used as reagents that investigated trapping for O_2^{*-}, OH*, e^-, and h^+, respectively. As illustrated in Figure 13, the 2-propanol, silver nitrate, and triethylamine have no significant effect on the photodegradation of DOX and TTC using the UiO-66@NH$_2$-DFNS, suggesting a negligible contribution from OH*, e^-, and h^+. In contrast, O_2^{*-} radicals appear to be the most likely reactive species involved in DOX and TTC photodegradation since 4-benzoquinone significantly suppresses the activity of UiO-66@NH$_2$-DFNS.[29] In agreement with these scavenger experiments, Figure 10 demonstrates that H_2O_2 has a negligible effect, which confirms that OH* is not involved in the reaction.

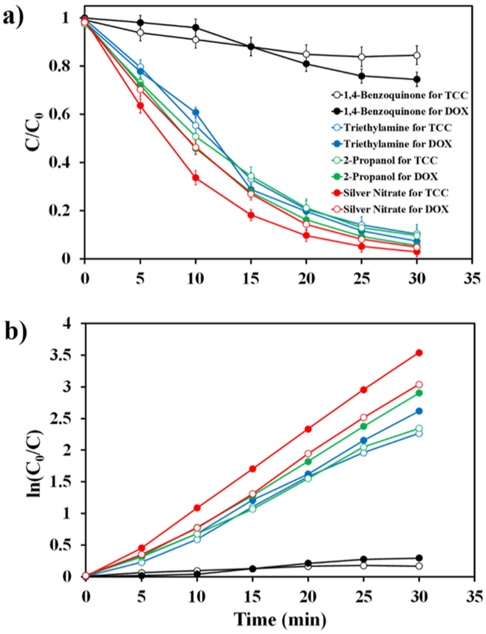

Figure 13. Effect of various scavengers on the DOX and TTC photodegradation using UiO-66@NH$_2$-DFNS. (a) C/C$_0$ versus time and (b) pseudo-first-order kinetic. Process condition: sample pH = 4.2, photocatalyst dose = 2.9 mg·mL^{-1}, DOX and TTC concentration = 200 mg·L^{-1}.

3.6. Reusability Investigation.

In the context of prolonged use, the importance of reusable photocatalysts cannot be overstated, as they play a crucial role in conserving both energy and costs. Five repeat degradation−washing-elution cycles under UV irradiation were conducted to verify the photocatalyst's stability. After each cycle, the UiO-66@NH$_2$-DFNS catalyst was centrifuged, washed/eluted with DDW/EtOH, dried at 80 °C, and reused. Mesoporous UiO-66@NH$_2$-DFNS is simultaneously regenerated into its initial form after washing/elution is completed. Based on the results of the reusability investigation, photodegradation efficiencies stayed above 85% (Figure 14a). The photodegradation efficiencies decreased slightly, which can be attributed to the loss of UiO-66@NH$_2$-DFNS during several degradation-washing-elution cycles. The amount of DOX/TTC eluted from the UiO-66@NH$_2$-DFNS surface, however, was lower than the quantification limit; therefore, they were not detected. This indicates that adsorption of antibiotics plays a minimal role in the proposed procedure, with photodegradation emerging as the predominant process.

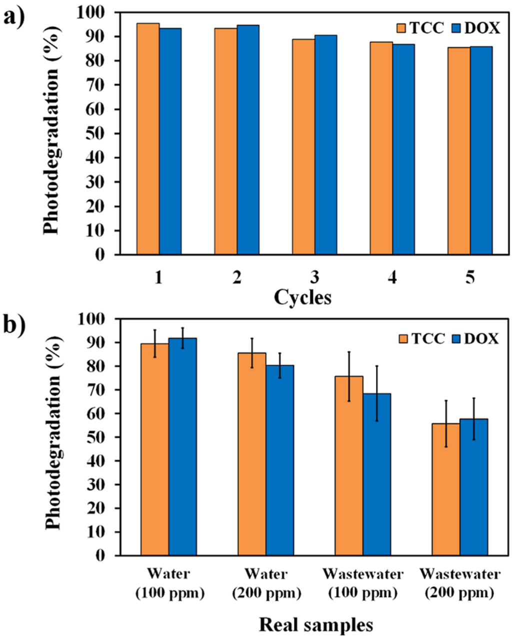

Figure 14. (a) Reusability tests of UiO-66@NH$_2$-DFNS and (b) its performance in two real samples, i.e., tap water and effluent of a pharmaceutical firm. Process conditions: sample pH = 4.2, photocatalyst dose = 2.9 mg·mL^{-1}, irradiation time = 30 min, DOX and TTC concentration = 100 and 200 mg·L^{-1}.

This reusability study shows that UiO-66@NH$_2$-DFNS can maintain its original photodegradation performance even after five cycles of use, rendering it an appealing choice for water and wastewater treatment applications.

3.7. Photodegradation Research on Actual Specimens.

Aiming to demonstrate the capability of the presented UiO-66@NH$_2$-DFNS nanocatalyst for the degradation of DOX and TTC, tap water and effluent discharge of a pharmaceutical firm (Daropakhsh Pharmaceutical Chemical, Karaj, Tehran, Iran) were employed as actual specimens, and no DOX or TTC was discovered. The photodegradation capability outcomes of UiO-66@NH$_2$-DFNS from actual samples which were spiked with 100 and 200 mg·L^{-1} DOX and TTC revealed the likely photodegradation results (Figure 14b). This indicates that the presence of substantial quantities of various interfering species (e.g., cations such as Ca^{2+}, Mg^{2+}, Na^+, K^+, and so on, anions like HCO^{3-}, Cl^-, SO_4^{2-}, PO_4^{3-},

Table 4. Comparison of UiO-66@NH_2-DFNS with Other Reported Nanocomposites in DOX and TTC Removal

nanocomposite	removal mechanism	pH	dose (mg·mL^{-1})	conc. (mg·L^{-1})	time (min)	kinetic constant	refs
birnessite	photocatalytic	8.0	0.67	50	30	NR[a]	76
Ce/Fe	catalytic	7.0	2.0	10	60	0.0232 (min^{-1})	77
graphene oxide@Fe−Cu−Ag	catalytic	2.0	3.0	50	30	0.0457 (min^{-1})	7
schwertmannite	catalytic	2.0	1.6	20	120	0.0540−0.1492 (min^{-1})	80
graphene oxide/Mg−Zn−Al	adsorptive	8.0	1.5	100	90	0.0021 (L·mg^{-1}·min^{-1})	78
syzygium cumini l. wood biochar	adsorptive	7.0	1.0	20	60	0.0300 (L·mg^{-1}·min^{-1})	79
UiO-66@NH_2-DFNS	photocatalytic	4.2	2.9	200	30	0.0929−0.1209 (min^{-1})	this work

[a] Not reported.

etc., and different pharmaceuticals and additives) in real-world samples does not impede the photodegradation process when employing UiO-66@NH_2-DFNS. Hence, we are of the opinion that UiO-66@NH_2-DFNS, as prepared, holds significant potential for use in the purification of water and wastewater.

3.8. Comparison with Other Reported Nanocomposites. Numerous efficient nanocomposites for the removal of DOX and TTC have been documented in the literature, as shown in Table 4, where their performance was assessed in comparison to the synthesized UiO-66@NH_2-DFNS.[7,76−80] A significant advantage of UiO-66@NH_2-DFNS over the reported adsorbents is its photocatalytic property.[78,79] These reported substrates only bind antibiotics to their surfaces through an adsorptive removal mechanism, which results in pollution transfer from large aqueous media to the solid substrate with a small area. Based on the data shown in Table 4, in comparison with catalytic and photocatalytic substrates, the proposed UiO-66@NH_2-DFNS accelerates the degradation of DOX and TTC by up to 200 mg·L^{-1} in only 30 min at moderate pH, which provides excellent photodegradation.[7,76,77,80] Additionally UiO-66@NH_2-DFNS stands out as a unique nanocomposite due to its favorable kinetic constants, rapid and straightforward synthesis process, and the ability to be reused up to five times without a notable decline in photodegradation efficiency.

4. CONCLUSIONS

This study successfully developed and characterized an innovative UiO-66 nanocomposite photocatalyst for the efficient photodegradation of TTC-class antibiotics, including DOX and TTC. The immobilization of UiO-66 on NH_2-DFNS was confirmed through characterization analyses, resulting in an excellent heterojunction, a narrow band gap energy, and a large specific surface area, all contributing to the enhanced photocatalytic performance.

Utilizing a CCD, various reaction variables were optimized, leading to the photocatalyst achieving a remarkable degradation efficiency of 97.2 ± 3.1 for aqueous media containing 200 mg·L^{-1} of DOX and TTC under defined optimal conditions: pH = 4.2, nanocomposite dose = 2.9 mg·mL^{-1}, and irradiation time = 30 min. The experimental results satisfy the model predictions (95.7 ± 2.2%).

The oxidation of DOX and TTC was found to be the primary degradation process, facilitated by superoxide radical anions on the UiO-66@NH_2-DFNS surface, derived from the oxidation of water and dissolved oxygen molecules. Kinetic showed that the experimental data followed a pseudo-first-order model and indicated that the surface reaction was the rate-determining step.

Our experiments demonstrated that the proposed materials exhibited significantly superior degradation of TTC-class antibiotics compared to other methods. The advantages included rapid degradation in just 30 min, moderate pH conditions, an excellent kinetic constant, ease and speed of synthesis, and a five-fold increase in reusability without a significant decrease in the photodegradation efficiency, resulting in excellent photodegradation performance using this unique nanocomposite.

■ AUTHOR INFORMATION

Corresponding Authors

Ali Ahmadpour − *Department of Chemical Engineering, Faculty of Engineering, Ferdowsi University of Mashhad, Mashhad 9177948944, Iran; Industrial Catalysts, Adsorbents and Environment Lab., Oil and Gas Research Institute, Ferdowsi University of Mashhad, Mashhad 9177948974, Iran*; Phone: +98-51-38805006; Email: Ahmadpour@um.ac.ir

Arash Arami-Niya − *Discipline of Chemical Engineering, Western Australian School of Mines: Minerals, Energy and Chemical Engineering, Curtin University, Perth, Western Australia 6845, Australia*; orcid.org/0000-0001-6450-0774; Phone: +61-8-9266-5482; Email: Arash.araminiya@curtin.edu.au

Authors

Fatemeh Deymeh − *Department of Chemical Engineering, Faculty of Engineering, Ferdowsi University of Mashhad, Mashhad 9177948944, Iran; Industrial Catalysts, Adsorbents and Environment Lab., Oil and Gas Research Institute, Ferdowsi University of Mashhad, Mashhad 9177948974, Iran*

Ali Allahresani − *Department of Chemistry, College of Sciences, University of Birjand, Birjand 9717434765, Iran*

Complete contact information is available at:
https://pubs.acs.org/10.1021/acs.iecr.3c02193

Author Contributions

Fatemeh Deymeh: conceptualization, methodology, investigation, writing—original draft, writing—review and editing, and visualization. **Ali Ahmadpour**: conceptualization, review and editing, supervision, and funding acquisition. **Ali Allahresani** and **Arash Arami-Niya**: conceptualization, review and editing, and advisor.

Notes

The authors declare no competing financial interest.

■ ACKNOWLEDGMENTS

The authors appreciate the support of the Ferdowsi University of Mashhad, Iran (grant no. 54010) for this work.

■ REFERENCES

(1) Shahat, A.; Kubra, K. T.; Salman, M. S.; Hasan, M. N.; Hasan, M. M. Novel Solid-State Sensor Material for Efficient Cadmium(II) Detection and Capturing from Wastewater. *Microchem. J.* **2021**, *164*, 105967.

(2) Awual, M. R. A Novel Facial Composite Adsorbent for Enhanced Copper(II) Detection and Removal from Wastewater. *Chem. Eng. J.* **2015**, *266*, 368−375.

(3) Hasan, M. N.; Shenashen, M. A.; Hasan, M. M.; Znad, H.; Awual, M. R. Assessing of Cesium Removal from Wastewater Using Functionalized Wood Cellulosic Adsorbent. *Chemosphere* **2021**, *270*, 128668.

(4) Hasan, M. M.; Salman, M. S.; Hasan, M. N.; Rehan, A. I.; Awual, M. E.; Rasee, A. I.; Waliullah, R. M.; Hossain, M. S.; Kubra, K. T.; Sheikh, M. C.; Khaleque, M. A.; Marwani, H. M.; Islam, A.; Awual, M. R. Facial Conjugate Adsorbent for Sustainable Pb(II) Ion Monitoring and Removal from Contaminated Water. *Colloids Surf., A* **2023**, *673*, 131794.

(5) Awual, M. R. Efficient Phosphate Removal from Water for Controlling Eutrophication Using Novel Composite Adsorbent. *J. Cleaner Prod.* **2019**, *228*, 1311−1319.

(6) Awual, M. R.; Hasan, M. M.; Islam, A.; Rahman, M. M.; Asiri, A. M.; Khaleque, M. A.; Sheikh, M. C. Introducing an Amine Functionalized Novel Conjugate Material for Toxic Nitrite Detection and Adsorption from Wastewater. *J. Cleaner Prod.* **2019**, *228*, 778−785.

(7) Hemmat, K.; Khodabakhshi, M. R.; Zeraatkar Moghaddam, A. Synthesis of Nanoscale Zero-Valent Iron Modified Graphene Oxide Nanosheets and Its Application for Removing Tetracycline Antibiotic: Response Surface Methodology. *Appl. Organomet. Chem.* **2021**, *35* (1), No. e6059.

(8) Rehan, A. I.; Rasee, A. I.; Awual, M. E.; Waliullah, R. M.; Hossain, M. S.; Kubra, K. T.; Salman, M. S.; Hasan, M. M.; Hasan, M. N.; Sheikh, M. C.; Marwani, H. M.; Khaleque, M. A.; Islam, A.; Awual, M. R. Improving Toxic Dye Removal and Remediation Using Novel Nanocomposite Fibrous Adsorbent. *Colloids Surf., A* **2023**, *673*, 131859.

(9) Moghaddam, A. Z.; Jazi, M. E.; Allahrasani, A.; Ganjali, M. R.; Badiei, A. Removal of Acid Dyes from Aqueous Solutions Using a New Eco-Friendly Nanocomposite of CoFe2O4Modified with Tragacanth Gum. *J. Appl. Polym. Sci.* **2020**, *137* (17), 48605.

(10) Yang, X.; Chen, Z.; Zhao, W.; Liu, C.; Qian, X.; Zhang, M.; Wei, G.; Khan, E.; Hau Ng, Y.; Sik Ok, Y. Recent Advances in Photodegradation of Antibiotic Residues in Water. *Chem. Eng. J.* **2021**, *405*, 126806−126830.

(11) Hoslett, J.; Ghazal, H.; Katsou, E.; Jouhara, H. The Removal of Tetracycline from Water Using Biochar Produced from Agricultural Discarded Material. *Sci. Total Environ.* **2021**, *751*, 141755−141765.

(12) Xing, Z. P.; Sun, D. Z. Treatment of Antibiotic Fermentation Wastewater by Combined Polyferric Sulfate Coagulation, Fenton and Sedimentation Process. *J. Hazard. Mater.* **2009**, *168* (2−3), 1264−1268.

(13) Li, Q.; Ji, M.; Li, X.; Song, H.; Wang, G.; Qi, C.; Li, A. Efficient Co-Removal of Copper and Tetracycline from Aqueous Solution by Using Permanent Magnetic Cation Exchange Resin. *Bioresour. Technol.* **2019**, *293*, 122068.

(14) Alonso, J. J. S.; El Kori, N.; Melián-Martel, N.; Del Río-Gamero, B. Removal of Ciprofloxacin from Seawater by Reverse Osmosis. *J. Environ. Manage.* **2018**, *217*, 337−345.

(15) Lan, L.; Kong, X.; Sun, H.; Li, C.; Liu, D. High Removal Efficiency of Antibiotic Resistance Genes in Swine Wastewater via Nanofiltration and Reverse Osmosis Processes. *J. Environ. Manage.* **2019**, *231*, 439−445.

(16) Wang, L.; Liu, Y.; Pang, D.; Song, H.; Zhang, S. Simultaneous Electrochemical Degradation of Tetracycline and Metronidazole through a High-Efficiency and Low-Energy-Consumption Advanced Oxidation Process. *Chemosphere* **2022**, *292*, 133469.

(17) Gao, G.; Zhang, X.; Wang, P.; Ren, Y.; Meng, X.; Ding, Y.; Zhang, T.; Jiang, W. Electrochemical Degradation of Doxycycline Hydrochloride on Bi/Ce Co-Doped Ti/PbO2 Anodes: Efficiency and Mechanism. *J. Environ. Chem. Eng.* **2022**, *10* (5), 108430.

(18) Yin, F.; Lin, S.; Zhou, X.; Dong, H.; Zhan, Y. Fate of Antibiotics during Membrane Separation Followed by Physical-Chemical Treatment Processes. *Sci. Total Environ.* **2021**, *759*, 143520−143528.

(19) Xu, Z.; Jia, Y.; Zhang, X.; Hu, S.; Luo, Y.; He, H.; Chen, B.; Huang, B.; Pan, X. Algal Organic Matter Accelerates the Photodegradation of Tetracycline: Mechanisms, Degradation Pathways and Product Toxicity. *Chem. Eng. J.* **2023**, *468*, 143724.

(20) Li, J.; Song, Y.; Wei, Z.; Wang, F.; Zhang, X.; Zhu, H.; Sheng, S.; Zou, H. Unique Kinetics Feature and Excellent Photocatalytic Performance of Tetracycline Photodegradation Using Yolk-Shell TiO2@void@TiO2:Eu3+. *Appl. Catal., A* **2023**, *650*, 119008.

(21) Huang, L.; Liu, H.; Wang, Y.; Zhang, T. C.; Yuan, S. Construction of Ternary Bi2O3/Biochar/g-C3N4 Heterojunction to Accelerate Photoinduced Carrier Separation for Enhanced Tetracycline Photodegradation. *Appl. Surf. Sci.* **2023**, *616*, 156509.

(22) Sivaranjani, P. R.; Syed, A.; Elgorban, A. M.; Bahkali, A. H.; Balakrishnaraja, R.; Varma, R. S.; Sudheer Khan, S. Fabrication of ternary nano-heterojunction via hierarchical deposition of α-Fe2O3 and β-La2S3 on cubic CoCr2O4 for enhanced photodegradation of doxycycline. *J. Ind. Eng. Chem.* **2023**, *118*, 407−417.

(23) Ding, R.; Ouyang, Z.; Zhang, X.; Dong, Y.; Guo, X.; Zhu, L. Biofilm-Colonized versus Virgin Black Microplastics to Accelerate the Photodegradation of Tetracycline in Aquatic Environments: Analysis of Underneath Mechanisms. *Environ. Sci. Technol.* **2023**, *57* (14), 5714−5725.

(24) Deymeh, F.; Ahmadpour, A.; Allahresani, A. Binary Antibiotics Degradation Employing an Efficient Direct Z-Scheme Ti(VI)-Salen Complex Loaded on Dendritic Fibrous Nano-Silica. *Water, Air, Soil Pollut.* **2023**, *234* (4), 263.

(25) Yang, L.; Yuan, C.; Chen, X.; Xue, W.; Cao, G.; Meng, S.; Bai, L. The Effect of Nitrification Inhibitors on the Aerobic Biodegradation of Tetracycline Antibiotics in Swine Wastewater. *Chemosphere* **2023**, *311*, 136849.

(26) Liu, M.; Gao, Y.; Wang, Y.; Li, Y.; Zou, D. Status and Opportunities in the Treatment of Tetracyclines from Aquatic Environments by Metal-Organic Frameworks (MOFs) and MOFs-Based Composites. *Mater. Today Chem.* **2022**, *26*, 101209−101230.

(27) Wu, S.; Hu, H.; Lin, Y.; Zhang, J.; Hu, Y. H. Visible Light Photocatalytic Degradation of Tetracycline over TiO2. *Chem. Eng. J.* **2020**, *382*, 122842−122852.

(28) Wang, C. C.; Wang, X.; Liu, W. The Synthesis Strategies and Photocatalytic Performances of TiO2/MOFs Composites: A State-of-the-Art Review. *Chem. Eng. J.* **2020**, *391*, 123601.

(29) Wang, Y. L.; Zhang, S.; Zhao, Y. F.; Bedia, J.; Rodriguez, J. J.; Belver, C. UiO-66-Based Metal Organic Frameworks for the Photodegradation of Acetaminophen under Simulated Solar Irradiation. *J. Environ. Chem. Eng.* **2021**, *9* (5), 106087−110697.

(30) Swetha, S.; Janani, B.; Khan, S. S. A Critical Review on the Development of Metal-Organic Frameworks for Boosting Photocatalysis in the Fields of Energy and Environment. *J. Cleaner Prod.* **2022**, *333*, 130164−130182.

(31) He, S.; Zhu, B.; Jiang, X.; Han, G.; Li, S.; Lau, C. H.; Wu, Y.; Zhang, Y.; Shao, L. Symbiosis-Inspired de Novo Synthesis of Ultrahigh MOF Growth Mixed Matrix Membranes for Sustainable Carbon Capture. *Proc. Natl. Acad. Sci. U.S.A.* **2022**, *119* (1), No. e2114964119.

(32) Zhu, B.; He, S.; Yang, Y.; Li, S.; Lau, C. H.; Liu, S.; Shao, L. Boosting Membrane Carbon Capture via Multifaceted Polyphenol-Mediated Soldering. *Nat. Commun.* **2023**, *14* (1), 1697.

(33) Ye, Q.; Xu, J. M.; Zhang, Y. J.; Chen, S. H.; Zhan, X. Q.; Ni, W.; Tsai, L. C.; Jiang, T.; Ma, N.; Tsai, F. C. Metal-Organic Framework Modified Hydrophilic Polyvinylidene Fluoride Porous Membrane for Efficient Degerming Selective Oil/Water Emulsion Separation. *npj Clean Water* **2022**, *5* (1), 23.

(34) Zeng, H.; He, S.; Hosseini, S. S.; Zhu, B.; Shao, L. Emerging Nanomaterial Incorporated Membranes for Gas Separation and

Pervaporation towards Energetic-Efficient Applications. *Adv. Membr.* **2022**, *2*, 100015.

(35) Fakhri, H.; Bagheri, H. Two Novel Sets of UiO-66@ Metal Oxide/Graphene Oxide Z-Scheme Heterojunction: Insight into Tetracycline and Malathion Photodegradation. *J. Environ. Sci.* **2020**, *91*, 222−236.

(36) Du, Q.; Wu, P.; Sun, Y.; Zhang, J.; He, H. Selective Photodegradation of Tetracycline by Molecularly Imprinted ZnO@ NH2-UiO-66 Composites. *Chem. Eng. J.* **2020**, *390*, 124614.

(37) Zhang, R.; Du, B.; Li, Q.; Cao, Z.; Feng, G.; Wang, X. α-Fe2O3 nanoclusters confined into UiO-66 for efficient visible-light photodegradation performance. *Appl. Surf. Sci.* **2019**, *466*, 956−963.

(38) Ghorbani, M.; Solaimany Nazar, A. R.; Frahadian, M.; Tangestaninejad, S. Fabrication of Novel ZnO@BiOBr/UiO-66-NH2 Core-Shell Heterojunction for Improved Tetracycline Degradation. *Appl. Surf. Sci.* **2023**, *612*, 155819.

(39) Lin, Z.; Wu, Y.; Jin, X.; Liang, D.; Jin, Y.; Huang, S.; Wang, Z.; Liu, H.; Chen, P.; Lv, W.; Liu, G. Facile Synthesis of Direct Z-Scheme UiO-66-NH2/PhC2Cu Heterojunction with Ultrahigh Redox Potential for Enhanced Photocatalytic Cr(VI) Reduction and NOR Degradation. *J. Hazard. Mater.* **2023**, *443*, 130195−130212.

(40) Man, Z.; Meng, Y.; Lin, X.; Dai, X.; Wang, L.; Liu, D. Assembling UiO-66@TiO2 Nanocomposites for Efficient Photocatalytic Degradation of Dimethyl Sulfide. *Chem. Eng. J.* **2022**, *431*, 133952−133962.

(41) Wei, T.; Zhao, B.; Zhou, Z.; Di, H.; Shumba, T.; Cui, M.; Zhou, Z.; Xu, X.; Qi, M.; Tang, J.; Ndungu, P. G.; Qiao, X.; Zhang, Z. Removal of Organics and Ammonia in Landfill Leachate via Catalytic Oxypyrolysis over MOF-Derived Fe2O3@SiO2-Al2O3. *Sep. Purif. Technol.* **2023**, *305*, 122467.

(42) Nikpour, S.; Ansari-Asl, Z.; Sedaghat, T. Fabrication and Characterization of Polystyrene/Fe-MOF Composite Beads for Iodine Uptake. *Inorg. Chem. Commun.* **2022**, *136*, 109141.

(43) Li, K.; Zou, S.; Jin, G.; Yang, J.; Dou, M.; Qin, L.; Su, H.; Huang, F. Efficient Removal of Selenite in Aqueous Solution by MOF-801 and Fe3O4/MOF-801: Adsorptive Behavior and Mechanism Study. *Sep. Purif. Technol.* **2022**, *296*, 121384.

(44) Grad, O.; Dan, M.; Barbu-Tudoran, L.; Tosa, N.; Lazar, M. D.; Blanita, G. MOF/Al2O3 Composites Obtained by Immobilization of MIL-53(Cr) or MIL-101(Cr) on γ-Alumina: Preparation and Characterization. *Microporous Mesoporous Mater.* **2023**, *353*, 112518.

(45) Cavka, J. H.; Jakobsen, S.; Olsbye, U.; Guillou, N.; Lamberti, C.; Bordiga, S.; Lillerud, K. P. A New Zirconium Inorganic Building Brick Forming Metal Organic Frameworks with Exceptional Stability. *J. Am. Chem. Soc.* **2008**, *130* (42), 13850−13851.

(46) Winarta, J.; Shan, B.; Mcintyre, S. M.; Ye, L.; Wang, C.; Liu, J.; Mu, B. A Decade of UiO-66 Research: A Historic Review of Dynamic Structure, Synthesis Mechanisms, and Characterization Techniques of an Archetypal Metal−Organic Framework. *Cryst. Growth Des.* **2020**, *20* (2), 1347−1362.

(47) Trushina, D. B.; Sapach, A. Y.; Burachevskaia, O. A.; Medvedev, P. V.; Khmelenin, D. N.; Borodina, T. N.; Soldatov, M. A.; Butova, V. V. Doxorubicin-Loaded Core−Shell UiO-66@SiO2Metal−Organic Frameworks for Targeted Cellular Uptake and Cancer Treatment. *Pharmaceutics* **2022**, *14* (7), 1325.

(48) Polshettiwar, V.; Cha, D.; Zhang, X.; Basset, J. M. High-Surface-Area Silica Nanospheres (KCC-1) with a Fibrous Morphology. *Angew. Chem., Int. Ed.* **2010**, *49* (50), 9652−9656.

(49) Singh, R.; Bapat, R.; Qin, L.; Feng, H.; Polshettiwar, V. Atomic Layer Deposited (ALD) TiO2 on Fibrous Nano-Silica (KCC-1) for Photocatalysis: Nanoparticle Formation and Size Quantization Effect. *ACS Catal.* **2016**, *6* (5), 2770−2784.

(50) Bayal, N.; Singh, R.; Polshettiwar, V. Nanostructured Silica−Titania Hybrid Using Dendritic Fibrous Nanosilica as a Photocatalyst. *ChemSusChem* **2017**, *10* (10), 2182−2191.

(51) Bayal, N.; Singh, B.; Singh, R.; Polshettiwar, V. Size and Fiber Density Controlled Synthesis of Fibrous Nanosilica Spheres (KCC-1). *Sci. Rep.* **2016**, *6* (1), 24888.

(52) Douglas, C. Montgomery. *Design and Analysis of Experiments*, 10th ed.; Wiley, 2019.

(53) Le, X.; Dong, Z.; Li, X.; Zhang, W.; Le, M.; Ma, J. Fibrous Nano-Silica Supported Palladium Nanoparticles: An Efficient Catalyst for the Reduction of 4-Nitrophenol and Hydrodechlorination of 4-Chlorophenol under Mild Conditions. *Catal. Commun.* **2015**, *59*, 21−25.

(54) Makuła, P.; Pacia, M.; Macyk, W. How To Correctly Determine the Band Gap Energy of Modified Semiconductor Photocatalysts Based on UV-Vis Spectra. *J. Phys. Chem. Lett.* **2018**, *9* (23), 6814−6817.

(55) Dong, F.; Wang, Z.; Li, Y.; Ho, W. K.; Lee, S. C. Immobilization of Polymeric G-C3N4 on Structured Ceramic Foam for Efficient Visible Light Photocatalytic Air Purification with Real Indoor Illumination. *Environ. Sci. Technol.* **2014**, *48* (17), 10345−10353.

(56) Zhang, Y.; Zhou, J.; Feng, Q.; Chen, X.; Hu, Z. Visible Light Photocatalytic Degradation of MB Using UiO-66/g-C3N4 Heterojunction Nanocatalyst. *Chemosphere* **2018**, *212*, 523−532.

(57) Kubra, K. T.; Hasan, M. M.; Hasan, M. N.; Salman, M. S.; Khaleque, M. A.; Sheikh, M. C.; Rehan, A. I.; Rasee, A. I.; Waliullah, R. M.; Awual, M. E.; Hossain, M. S.; Alsukaibi, A. K. D.; Alshammari, H. M.; Awual, M. R. The Heavy Lanthanide of Thulium(III) Separation and Recovery Using Specific Ligand-Based Facial Composite Adsorbent. *Colloids Surf., A* **2023**, *667*, 131415.

(58) Brunauer, S.; Emmett, P. H.; Teller, E. Adsorption of Gases in Multimolecular Layers. *J. Am. Chem. Soc.* **1938**, *60* (2), 309−319.

(59) Ambroz, F.; Macdonald, T. J.; Martis, V.; Parkin, I. P. Evaluation of the BET Theory for the Characterization of Meso and Microporous MOFs. *Small Methods* **2018**, *2* (11), 1800173.

(60) Awual, M. R.; Rahman, I. M. M.; Yaita, T.; Khaleque, M. A.; Ferdows, M. PH Dependent Cu(II) and Pd(II) Ions Detection and Removal from Aqueous Media by an Efficient Mesoporous Adsorbent. *Chem. Eng. J.* **2014**, *236*, 100−109.

(61) Hasan, M. N.; Salman, M. S.; Hasan, M. M.; Kubra, K. T.; Sheikh, M. C.; Rehan, A. I.; Rasee, A. I.; Awual, M. E.; Waliullah, R. M.; Hossain, M. S.; Islam, A.; Khandaker, S.; Alsukaibi, A. K. D.; Alshammari, H. M.; Awual, M. R. Assessing Sustainable Lutetium(III) Ions Adsorption and Recovery Using Novel Composite Hybrid Nanomaterials. *J. Mol. Struct.* **2023**, *1276*, 134795.

(62) Salman, M. S.; Hasan, M. N.; Hasan, M. M.; Kubra, K. T.; Sheikh, M. C.; Rehan, A. I.; Waliullah, R. M.; Rasee, A. I.; Awual, M. E.; Hossain, M. S.; Alsukaibi, A. K. D.; Alshammari, H. M.; Awual, M. R. Improving Copper(II) Ion Detection and Adsorption from Wastewater by the Ligand-Functionalized Composite Adsorbent. *J. Mol. Struct.* **2023**, *1282*, 135259.

(63) Hasan, M. M.; Kubra, K. T.; Hasan, M. N.; Awual, M. E.; Salman, M. S.; Sheikh, M. C.; Rehan, A. I.; Rasee, A. I.; Waliullah, R. M.; Islam, M. S.; Khandaker, S.; Islam, A.; Hossain, M. S.; Alsukaibi, A. K. D.; Alshammari, H. M.; Awual, M. R. Sustainable Ligand-Modified Based Composite Material for the Selective and Effective Cadmium(II) Capturing from Wastewater. *J. Mol. Liq.* **2023**, *371*, 121125.

(64) Aghajanzadeh, M.; Zamani, M.; Molavi, H.; Khieri Manjili, H.; Danafar, H.; Shojaei, A. Preparation of Metal−Organic Frameworks UiO-66 for Adsorptive Removal of Methotrexate from Aqueous Solution. *J. Inorg. Organomet. Polym. Mater.* **2018**, *28* (1), 177−186.

(65) Du, X.; He, J. Fine-Tuning of Silica Nanosphere Structure by Simple Regulation of the Volume Ratio of Cosolvents. *Langmuir* **2010**, *26* (12), 10057−10062.

(66) Duma, Z. G.; Dyosiba, X.; Moma, J.; Langmi, H. W.; Louis, B.; Parkhomenko, K.; Musyoka, N. M. Thermocatalytic Hydrogenation of CO2 to Methanol Using Cu-ZnO Bimetallic Catalysts Supported on Metal−Organic Frameworks. *Catalysts* **2022**, *12* (4), 401−416.

(67) Wang, J.; He, Y.; Wan, X.; Xie, F.; Sun, Y.; Li, T.; Xu, Q.; Zhao, D.; Qu, Q. Core-Shell Metal-Organic Framework/Silica Hybrid with Tunable Shell Structure as Stationary Phase for High Performance Liquid Chromatography. *J. Chromatogr. A* **2023**, *1705*, 464164.

(68) Bouhrara, M.; Ranga, C.; Fihri, A.; Shaikh, R. R.; Sarawade, P.; Emwas, A. H.; Hedhili, M. N.; Polshettiwar, V. Nitridated Fibrous Silica (KCC-1) as a Sustainable Solid Base Nanocatalyst. *ACS Sustain. Chem. Eng.* **2013**, *1* (9), 1192−1199.

(69) Cao, Z.; Zhang, T.; Ren, P.; Cao, D.; Lin, Y.; Wang, L.; Zhang, B.; Xiang, X. Doping of Chlorine from a Neoprene Adhesive Enhances Degradation Efficiency of Dyes by Structured TiO2-Coated Photocatalytic Fabrics. *Catalysts* **2020**, *10* (1), 69−85.

(70) Li, S.; Hu, C.; Peng, Y.; Chen, Z. One-Step Scalable Synthesis of Honeycomb-like g-C3N4 with Broad Sub-Bandgap Absorption for Superior Visible-Light-Driven Photocatalytic Hydrogen Evolution. *RSC Adv.* **2019**, *9* (56), 32674−32682.

(71) Delekar, S. D.; Dhodamani, A. G.; More, K. V.; Dongale, T. D.; Kamat, R. K.; Acquah, S. F. A.; Dalal, N. S.; Panda, D. K. Structural and Optical Properties of Nanocrystalline TiO2 with Multiwalled Carbon Nanotubes and Its Photovoltaic Studies Using Ru(II) Sensitizers. *ACS Omega* **2018**, *3* (3), 2743−2756.

(72) Zhao, J.; Hidaka, H.; Takamura, A.; Pelizzetti, E.; Serpone, N. Photodegradation of surfactants. 11. .zeta.-Potential measurements in the photocatalytic oxidation of surfactants in aqueous titania dispersions. *Langmuir* **1993**, *9* (7), 1646−1650.

(73) Mohammadi, A.; Pourmoslemi, S. Enhanced Photocatalytic Degradation of Doxycycline Using a Magnetic Polymer-ZnO Composite. *Water Sci. Technol.* **2018**, *2017* (3), 791−801.

(74) Li, D.; Hua, T.; Li, X.; Cheng, J.; Du, K.; Hu, Y.; Chen, Y. In-Situ Fabrication of Ionic Liquids/MIL-68(In)−NH2 Photocatalyst for Improving Visible-Light Photocatalytic Degradation of Doxycycline Hydrochloride. *Chemosphere* **2022**, *292*, 133461.

(75) Mehrotra, K.; Yablonsky, G. S.; Ray, A. K. Kinetic Studies of Photocatalytic Degradation in a TiO2 Slurry System: Distinguishing Working Regimes and Determining Rate Dependences. *Ind. Eng. Chem. Res.* **2003**, *42* (11), 2273−2281.

(76) Chen, Z.; Ou, D.; Gu, G.; Gao, S.; Li, X.; Hu, C.; Liang, X.; Zhang, Y. Removal of Tetracycline from Water by Catalytic Photodegradation Combined with the Microalga Scenedesmus Obliquus and the Responses of Algal Photosynthesis and Transcription. *J. Environ. Manage.* **2023**, *326*, 116693.

(77) Han, W.; Shou, J.; Yang, Y.; Chen, L.; Zhang, L.; Chen, Y.; Tu, X.; Jin, D.; Zhang, S.; Chang, Y.; Zheng, H. High-Efficient Removal of Tetracycline in Water via Porous Magnetic Ce/Fe Photocomposite under Visible Light. *J. Rare Earths* **2022**. In press.

(78) Rahman, N.; Raheem, A. Graphene Oxide/Mg-Zn-Al Layered Double Hydroxide for Efficient Removal of Doxycycline from Water: Taguchi Approach for Optimization. *J. Mol. Liq.* **2022**, *354*, 118899.

(79) Srivastava, A.; Dave, H.; Prasad, B.; Maurya, D. M.; Kumari, M.; Sillanpää, M.; Prasad, K. S. Low Cost Iron Modified Syzygium Cumini l. Wood Biochar for Adsorptive Removal of Ciprofloxacin and Doxycycline Antibiotics from Aqueous Solution. *Inorg. Chem. Commun.* **2022**, *144*, 109895.

(80) Tian, Y.; Liu, F.; Sun, B.; Tong, Z.; Fu, P.; Zhang, J.; Bi, W.; Xu, S.; Pei, G. Efficient Removal of Doxycycline Using Schwertmannite as a Heterogeneous Fenton-like Catalyst over a Wide PH Range. *J. Environ. Chem. Eng.* **2023**, *11* (2), 109441.

https://doi.org/10.1021/acs.iecr.3c02193